


Article

Carbide Nanoparticle Dispersion Techniques for Metal Powder Metallurgy

Bahrum Prang Rocky¹, Christopher R. Weinberger², Steven R. Daniewicz¹ and Gregory B. Thompson^{1,*} 

¹ Department of Metallurgical and Materials Engineering, The University of Alabama, Tuscaloosa, AL 35401, USA; aprocky@ua.edu (B.P.R.); srdaniewicz@eng.ua.edu (S.R.D.)

² Department of Mechanical Engineering, Colorado State University, Fort Collins, CO 80523, USA; Chris.Weinberger@colostate.edu

* Correspondence: gthompson@eng.ua.edu; Tel.: +1-205-348-1589

Abstract: Nanoparticles (NP) embedded into a matrix material have been shown to improve mechanical properties such as strength, hardness, and wear-resistance. However, the tendency of NPs to agglomerate in the powder mixing process is a major concern. This study investigates five different mechanochemical processing (MCP) routes to mitigate agglomeration to achieve a uniform dispersion of ZrC NPs in an Fe-based metal matrix composite. Our results suggest that MCP with only process controlling agents is ineffective in avoiding aggregation of these NPs. Instead, the uniformity of the carbide NP dispersion is achieved by pre-dispersing the NPs under ultrasonication using suitable surfactants followed by mechanically mixing of the NPs with iron powders in an alcohol solvent which is then dried. High-energy MCP is then used to embed the NPs within the powders. These collective steps resulted in a uniform dispersion of ZrC in the sintered (consolidated) Fe sample.

Keywords: powder metallurgy; carbide nanoparticle; nanoparticle dispersion; strengthening of metals; metal alloying; mechanochemical process; high-energy ball-milling



Citation: Rocky, B.P.; Weinberger, C.R.; Daniewicz, S.R.; Thompson, G.B. Carbide Nanoparticle Dispersion Techniques for Metal Powder Metallurgy. *Metals* **2021**, *11*, 871. <https://doi.org/10.3390/met11060871>

Academic Editor: Martin Heilmaier

Received: 31 March 2021

Accepted: 21 May 2021

Published: 26 May 2021

Publisher's Note: MDPI stays neutral with regard to jurisdictional claims in published maps and institutional affiliations.



Copyright: © 2021 by the authors. Licensee MDPI, Basel, Switzerland. This article is an open access article distributed under the terms and conditions of the Creative Commons Attribution (CC BY) license (<https://creativecommons.org/licenses/by/4.0/>).

1. Introduction

Different microparticles or nanoparticles (NPs) are used in metals to improve their strength, hardness, fracture toughness, durability, and corrosion resistance [1–7]. Besides mechanical properties, these particles can also influence chemical partitioning behavior within the material. For example, nano-precipitates in steels have been reported to be traps for hydrogen which could result in reducing hydrogen embrittlement and improving hydrogen tolerance [8–12]. In many cases, whether mechanical or chemical influence, the composition of the nano-particulate phase is crucial. In some cases, these particulates do not necessarily achieve the desired structure and/or composition from a precipitation sequence within the matrix material itself. In such cases, the dispersion of particulates with a tailored phase is needed through a powder metallurgy route. Often the size of these tailored particulates requires the blending of NPs with micron-scale powders. A critical requirement is a means to uniformly disperse such NPs. Achieving a uniform dispersion requires overcoming the natural tendency of the NPs to agglomerate during mixing [13–21].

In powder metallurgy, mechanical ball-milling has been extensively applied to process coarse materials into fine powders and/or to produce alloy metals uniformly [20,22–26]. This imparted energy from milling refines the grain sizes, develops crystalline and quasicrystalline materials, disperses micro or nanoparticles, mechano-synthesizes new alloys, and so forth [23,27–30]. While high-energy ball-milling can readily grind larger particles to improve their uniformity during mixing [22,29], such milling causes several concerns for finer particles. These finer particle effects include agglomeration, cold-welding, fracturing, rewelding of prior pulverized powders, and oxidation [1,20,23,25–28,31,32]. To mitigate such issues, process controlling agents (PCAs) are used [26]. Nonpolar organic

hydrocarbon compounds, such as benzene, toluene, hexane, heptane, and many others are commonly applied as PCAs [22,33,34]. Organic PCA compounds generally adsorbed onto the particles' surfaces resulting in minimum surface contact between the particles [32,34]. Although beneficial towards preventing some of the aforementioned issues, it should be noted that the decomposition of the PCA adds by-products of carbon, hydrogen, nitrogen, and oxygen into the system which, even at their low concentration levels, will be a source of impurities within the mixture. Dependent upon the matrix elements, these contaminants can facilitate forming carbides, hydrides, nitrides, and oxides [32]. Hence, PCA selection is an important factor in any mechanochemical alloying.

In this work, we aim to promote the formation of fine carbide dispersions in iron-based alloys to achieve uniformity of NPs within the matrix. Although many researchers have conducted mechanochemical processing (MCP) for NP dispersions [14,16–18,21,35], agglomeration is still persistently reported. Here, we describe different processing routes to mitigate such issues through combinations of stearic acid as a PCA [1,4,22–24,26] and the use of polyethyleneimine (PEI) as a surfactant [36–38], Figure 1, for the NPs. While prior reports [24,39,40] have shown that ball-milling alone is insufficient in breaking the powders/particles apart to yield a uniform dispersion, by combining the PCA and PEI, the ability to reduce this aforementioned NP agglomeration before and during milling will be explored. Since PCAs and PEI have low melting (T_m) and boiling points (with the T_m of stearic acid = 69.3 °C and T_m of PEI = 75 °C), they readily evaporate or melt from frictional heat created by ball-milling or the direct sintering processes. Thus, a crucial issue will be how the PCA and surfactant evolve in the particles' dispersibility during milling.

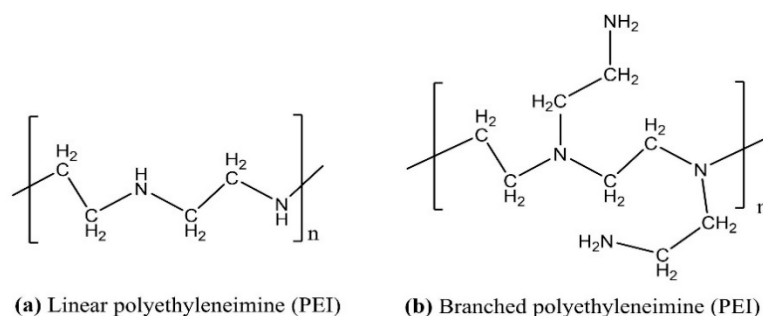


Figure 1. Linear (a) and branched (b) polyethyleneimine (PEI) used as a surfactant for the powders.

2. Materials and Methods

2.1. Machines and Materials

A Spex 8000 Mixer Mill with 8004 Tungsten Carbide Vials and Balls (Spex® SamplePrep, Metuchen, NJ, USA) were used for low-energy and short-term ball-milling. In addition, a Retsch MM500 Mixer Mill with stainless steel jars and balls (Verder Scientific, Inc., Newtown, PA, USA) was used for high-energy ball-milling. In both milling processes, a Unilab Pro SP glovebox (M. Braun, Inc., Stratham, NH, USA) filled with Ar and operated at <0.2 ppm O₂ and <0.5 ppm H₂O provided a handling and transfer environment for the powders in a post-milling state. A Carver Bench Top Manual 4350 Pellet Press (Carver, Inc., Wabash, IN, USA) and Retsch PP35 Pellet Press (Verder Scientific, Inc., Newtown, PA, USA) were employed for pressing the milled powders into green compact pellets.

The starting matrix powders were milled from 6–10 µm diameter Fe powders (purity ≥99.5%) with 60 nm diameter ZrC NPs (purity ≥97%). The powders were acquired from Alfa Aesar and/or SkySpring Nanomaterials, Inc. (Houston, TX, USA), respectively. Figure 2 shows the morphology of the initial Fe powders and ZrC NPs. The Fe particles were mostly spherical in shape with varied sizes (Figure 2a) with the ZrC NPs found to be 'clumped' into larger particles (Figure 2b). The PCA stearic acid (purity ≥98%) was purchased from BeanTown Chemical (Hudson, NH, USA). American Chemical Society (ACS) grade ethanol was employed as a solvent mixing solution (VWR International, LLC., Radnor, PA, USA) as will be discussed below. The surface polyethyleneimine (PEI) with

purity $\geq 99\%$, both linear and branched (Figure 1), was acquired from BeanTown Chemical (Hudson, NH, USA).

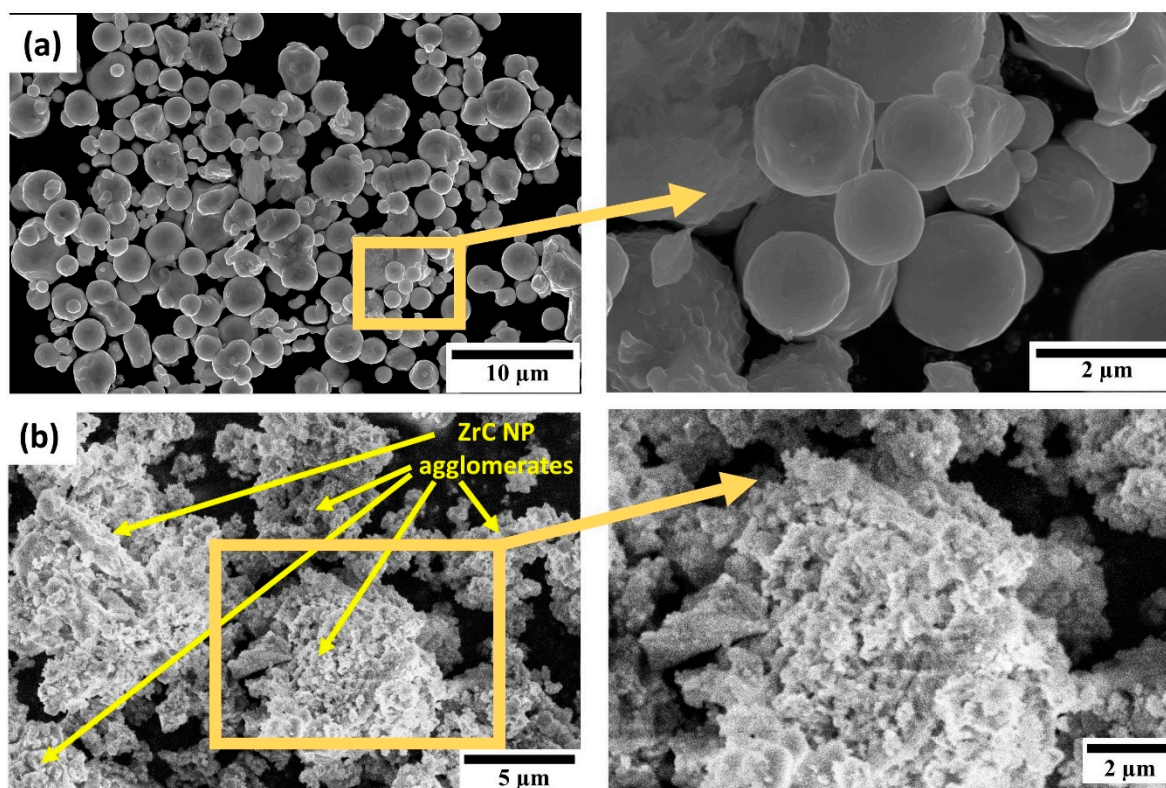


Figure 2. SEM (scanning electron microscopy) micrographs of (a) 6–10 μm Fe and (b) 60 nm ZrC nanoparticles.

A Bruker D8 X-ray diffractometer (Bruker, Billerica, MA, USA), JSM-7000F Field Emission Scanning Electron Microscope (JEOL Ltd., Peabody, MA, USA), and an Apreo 2 Scanning Electron Microscope (SEM) from ThermoFisher Scientific Inc. (Waltham, MA, USA) were used for probing the structural and chemical characteristics of the materials.

2.2. Different NP Dispersion Processing Routes

This paper reports on five different processing routes to disperse the NPs into a powder metallurgy derived consolidated Fe matrix. To that end, these are schematically drawn as various processing routes in Figure 3, with color designations to each route that are subsequently described in the following sub-section headers. The findings from each of these routes are then given in the Results section of the paper whereupon they are then expanded upon in the Discussion section.

2.2.1. Route-1 (Red): Low vs. High-Energy Ball-Milling NPs Directly with Fe Powders

This MCP approach was performed to assess the milling energy differences on the NP dispersions. Here the Spex's and Retsch's mills provide translational motion of 1060 cycles/min and 2100 cycles/min, respectively, creating a low-energy and high-energy processing path. A ball-to-powder ratio (BPR) of 3:1 to 5:1 was used for both mills. Based upon prior studies [4,22,24,26,40,41], various amounts of stearic acid ranged from 0 to 4 wt.% were added prior to milling. As will be shown and discussed in the Results, the Spex mill's lower energy was found to be less effective in reducing the particle agglomeration and adequately dispersing the NPs uniformly within the matrix. The Retsch mixer mill (with its higher milling energy) was found to be more effective and consequently became the primary means for milling all subsequent routes involving changes in the ZrC NP concentrations as well as other PCA/surfactant concentration modifications.

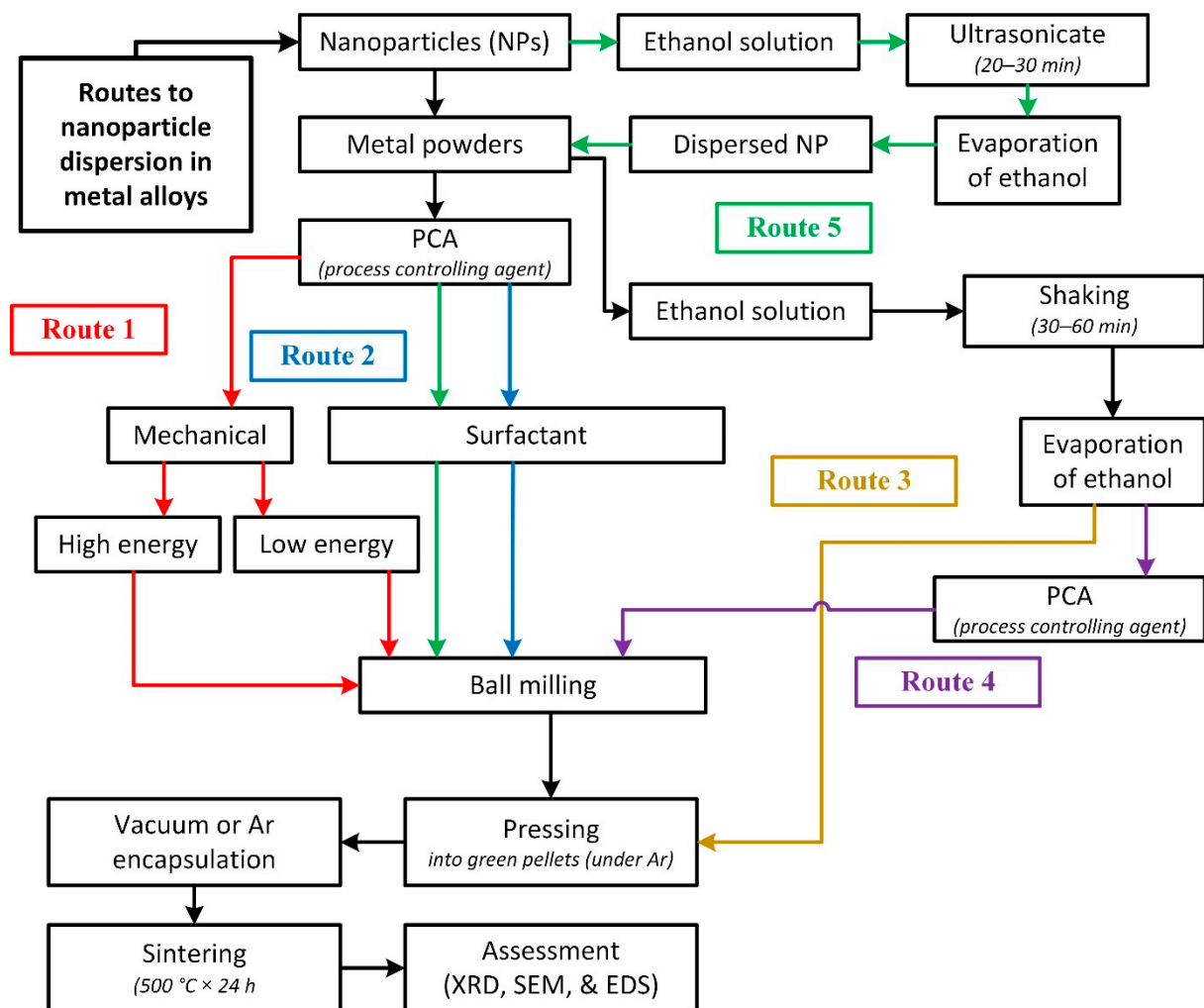


Figure 3. Flowchart diagram for different routes with the mechanochemical powder processing. XRD: X-ray Diffraction. EDS: energy-dispersive X-ray spectroscopy.

2.2.2. Route-2 (Blue): High-Energy Ball-Milling with Direct Surfactant Additions to NPs and Fe Powders

In Route 2, the ZrC NPs with 0.5 to 2 wt.% polyethyleneimine (PEI) and 2% stearic acid were directly mixed with the Fe powders followed by Retsch high-energy ball-milling. As shown in Figure 3, various process-based steps were then explored to identify the optimal mixing amounts of both surfactant and the sequence of mixing/milling to alter the ZrC dispersion. Within this route we also studied the effects regarding the duration of milling time on crystallite sizes and their link to promoting a uniform dispersion.

2.2.3. Route-3 (Gold): Mixing of the Powders via Liquid Solution

As will be shown and discussed below, the direct milling of the NPs with the Fe powders in Route 2 did not result in a uniform dispersion. Thus, in Route 3, the Fe powders and ZrC NPs were mixed in ethanol plus 2 wt.% PEI solution. The ethanol was 2× (by volume) the amount of the added powders. The solid powders/NPs and liquid were then mechanically shaken up to 60 min to uniformly disperse the powders with the NPs in the liquid solution whereupon the ethanol was evaporated by drying the solution in a fume hood at ambient temperature or under a warm hotplate (65 ± 5 °C) to accelerate the evaporation process. After drying, the particulates were either directed pressed and sintered or underwent an additional mechanical shaking at 20 Hz for 1 h and then pressed and sintered.

2.2.4. Route-4 (Purple): Mechanochemical Processing on Solution-Mixed Powders

This route is similar to Route 4 but has an additional step of ball-milling the dried powders from the ethanol solution with 2% stearic acid to prevent cold-welding during the ball milling process.

2.2.5. Route-5 (Green): Mechanochemical Processing of Dispersed NPs

Route 5 uses the ethanol methods of routes 3 or 4 but now only places the NPs into the alcohol solution with 2 wt.% PEI. The advantage of this route is a significant reduction of ethanol quantity used, which reduces the evaporation time as well as ensures the PEI is directly contacted by the NPs and no other powders. Furthermore, ultrasonication can now be applied to these NPs which will enable the PEI to cover the NPs more effectively. The PEI was first mechanically stirred with ethanol after which the ZrC NPs were added with the amount of ethanol being 10× the number of NPs (by weight). This solution was then subjected to ultrasonication for 30 min. Please note that the ultrasonication was performed in intervals of 5 min followed by a pause for 5 min to avoid overheating the solution until a total of 30 min of ultrasonication was achieved. Since the dispersion of the NPs by ultrasonication will have a finite time before agglomeration, we explored three methods to separate the NPs from the alcohol solution. The first two involved ambient and accelerated evaporation under a fume hood as done in routes 3 and 4. The other means was by centrifuging the particles at 2000 rev./min, which separates the NPs from the ethanol. Although this latter method quickly achieved phase separation, it also resulted in rapid re-agglomeration and was ultimately abandoned as a viable method. The accelerated evaporation by the hotplate (drying) was found to be the most effective means of removing the NPs from the ethanol solution. The dried NPs, which have the PEI coverage over their surfaces via ultrasonication, were then milled with the Fe powders with the addition of 1 wt.% steric acid to prevent cold-welding.

In all the routes above where milling was employed, the mixtures were milled for 4 to 6 h. This was performed at 1 h milling intervals at 30 Hz. Milling ceased between each interval for 1 h to reduce excessive frictional heat generation. After milling, the Fe powder's milling container was opened in an inert glove box since the milled powders can become pyrophoric. These powders were also loaded and pressed in the same inert glove box.

2.3. Consolidation of Powder Mixture

The various process route powders were consolidated into pellets using either a Carver Bench Top Manual Pellet Press (Model 4350) that compressed 10 mm diameter × 5 mm thick pellets (final size) at 5 metric tons of pressure for 5 min or using a Retsch Pellet Press (PP35) that produced 30 mm diameter × 5 mm thick pellets (final size) under 30 metric tons of pressure for 120 s. After pressing, the green compact pellets were encapsulated in quartz tubes under a vacuum (10^{-3} Torr) or an inert Ar atmosphere (75 Torr). The encapsulated pellets were heated at 500 °C for 24 h to sinter the powders together such that the pellets could be metallographically polished and imaged. While this sintering method will not achieve near full density (as no pressure was applied during heating), it was sufficient for the aims of this study, which was to have a consolidated material to evaluate the distribution of the NPs within the matrix phase. Subsequent studies are planned to use the powder processing routes reported here that lead to an optimal NP dispersion where hot isostatic pressing and/or spark plasma sintering can then facilitate near full density consolidation.

2.4. Analyses and Characterization

X-ray Diffraction (XRD) analysis was performed using a Bruker D8 with a Cu X-ray source operated at 40 kV and 40 mA current. The scans were performed in the Bragg-Brentano configuration between 15° to 125° two-theta by wide-angle X-ray scattering (WAXS).

For scanning electron microscopy (SEM) imaging, both the Thermo Fisher Apreo SEM and JEOL 7000 SEM were employed at low beam acceleration voltages (<10 keV) and probe currents (13 pA to 6.4 nA) to resolve the carbide NPs with higher acceleration voltages (20 keV) and currents (6.4–20 nA) for energy-dispersive X-ray spectroscopy (EDS) quantification and elemental mapping. Although the end-produced samples span sizes of several millimeters, the SEM characterization dictates imaging at a length scale of a few microns to resolve the NPs (which are sub-micron in size) within the microstructure. Consequently, several micrographs were taken over each sample to ensure that the images presented in this paper are representative of the dispersions noted for each processing route.

3. Results

3.1. Assessments of Route 1: Low vs. High-Energy Ball-Milling NPs Directly with Fe Powders

In this process, two different ball-milling methods were applied to assess if direct milling of the Fe powders with the NPs would directly yield a uniform dispersion. As would be expected, increased milling times resulted in smaller crystallite sizes of the powders, with the crystallite sizes being proportional to the impacted energy of the milling mill used. The crystallite sizes were calculated by the Scherrer method [42] using the {110} Fe planes with the results provided in Figure 4. Comparing the same milling time for each unit, the Spex mill reduced the crystallite sizes from ≈ 40 nm to ≈ 26 nm (2 h), Figure 4a, whereas the Retsch mill reduced the crystallite sizes from ≈ 40 nm to ≈ 11 nm (2 h), Figure 4b, with the periodic changes of the crystallite sizes over various times for both mills graphically represented in Figure 4c.

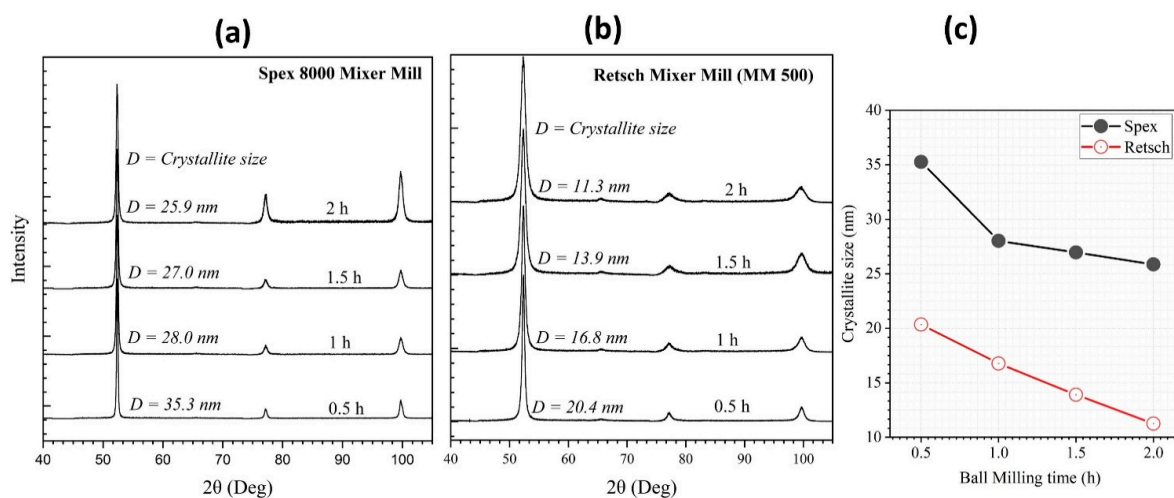


Figure 4. Comparison of mechanical alloying—(a,b) represent XRD (X-ray Diffraction) plots showing peak broadening from the {110} plane ($2\theta \approx 52^\circ$) of the metal powders using either the Spex or Retsch mill, respectively, and (c) the change in the crystallite size (Scherrer analysis) with milling time by each mill.

In this route, we varied the steric acid from 0 to 4 wt.%. In the case of no steric acid, we found that a small fraction of powders, after any milling time in either mill, were cold-welded to the stainless milling balls and container. Increasing the steric acid above 1% was found to be sufficient to mitigate this cold-welding issue. However, additions above 2 wt.% resulted in the powders becoming too ‘wet’ causing them to exhibit a ‘goosey’ or ‘mud-like’ property characteristics that was not conducive to ball-milling. All subsequent mills were performed with a steric acid addition between 1 to 2 wt.%.

Figure 5a,b are representative SEM micrographs of the Fe-5 vol.% ZrC, with the bright contrast associated with the carbide NPs. This was confirmed by EDS but not shown for brevity. In both milling states, the direct milling of the NPs with the Fe powders does not result in a uniform dispersion. Rather, one can note regions where the NPs are still agglomerated together in the consolidated matrix. These regions appear to be

both in the interior of the grains as well as at the grain boundaries where the Fe powders sintered together. One notable difference was the qualitative observation that the Restch mill was able to disperse more of the agglomerated particles throughout the sample, evident by a higher number of bright contrast features over the same field of view between the two milling experiments. This difference in dispersion is contributed to the higher imparted energy offered by this mill that helped break-up and separate clumps of NPs. This processing route demonstrated that a surfactant would most likely be needed to help separate the NPs from each other as mechanical milling alone is insufficient to break-apart the NP agglomerates and disperse the NPs uniformly throughout the consolidated Fe matrix.

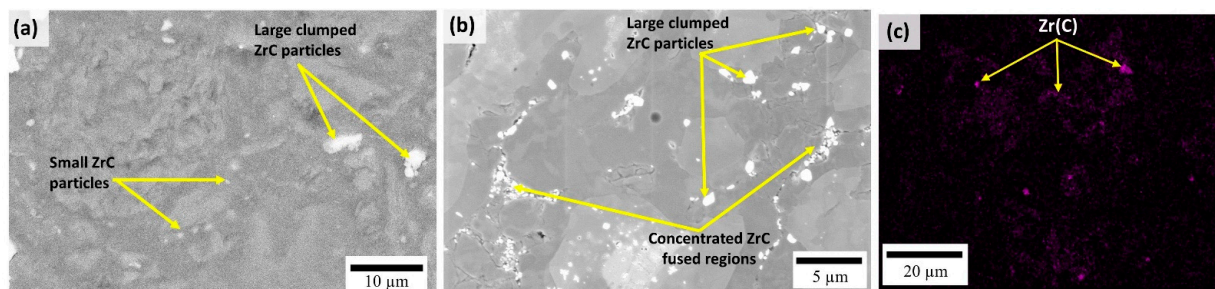


Figure 5. Secondary electron SEM micrographs of the sintered Fe-5 vol.% ZrC alloys milled by (a) Spex for 2 h (b) Retsch for 2 h, (c) EDS (energy-dispersive X-ray spectroscopy) elemental map of the Zr signal. The bright contrast is from the agglomerated ZrC NPs.

3.2. Assessments of Route 2: High-Energy Ball-Milling with Direct Surfactant Additions to the NPs and Fe Powders

Based on the outcomes of Route 1, the Retsch milling system (with its higher ball-milling energy) coupled with PEI as a surfactant was added to a mixture of Fe powders with 5 vol.% of NPs. The PEI had a degree of polymerization (DP) between 600–1000; note that if the DP is too high, the polymer is too large for dispersion purposes. We also have investigated both linear, branched, and mixtures of both, and no noticeable differences in the dispersions were observed. Recognizing that the Retsch mill was able to yield smaller crystallites in the same milling time as the Spex mill, Figure 4, as well as a perceived improvement in the NP dispersity within the matrix, Figure 5b, Route 2 expanded the milling times to further optimize these outcomes in parallel with the PEI addition. With increasing the milling to 8 h, the broadening of the XRD peaks, Figure 6a, and corresponding reduction of the Scherrer estimate crystallite size, Figure 6b, is seen as a function of these milling times. Although the crystallite sizes continually decreased with milling time, a reduction in the rate of crystallite size is relatively stagnant between 4 to 7 h with the crystallite size being on the order of 10 ± 1 nm.

Accompanying the reduced crystallite size is a change in the lattice strain that is imparted to the crystallites because of the high-energy ball-milling. Using the Williamson-Hall method, Figure 6c is a plot of the strain percentage as a function of milling time as measured from the peak broadening of Fe's body-centered cubic (BCC) {110}, {200} and {211} reflections in Figure 6a. As would be expected, the strain increased with milling time from the imparted deformation energy and reached a maximum value of $\approx 2.44\%$ after 6 h. Interestingly, the strain reduced to $\approx 1.7\%$ for subsequent milling times. Recognizing that a small crystallite size is present, and a minimal size change occurred over longer milling periods, it was concluded that milling within 5 ± 1 h would be sufficient for all further milling for the other routes. Please note that in the estimate of the Scherrer crystallite size and strain the instrument broadening effects from the diffractometer were measured from a coarse grain (>10 µm) Fe standard for the equivalent reflected BCC peaks. The full width half maximum values (FWHM) for this coarse grain XRD scan used the same reflections that were then subtracted from the milled powder's FWHM values to improve the accuracy of the given estimates.

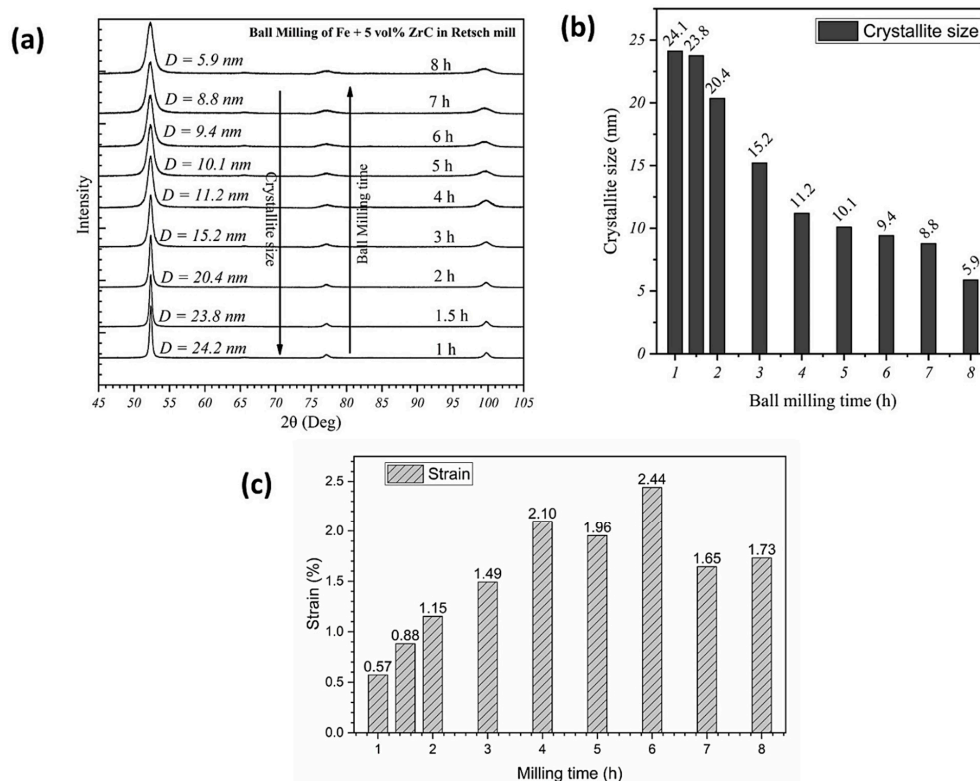


Figure 6. Effect of ball-milling time on crystallite sizes—(a) XRD patterns showing peak widths, (b) crystallite size (by Scherrer analysis) as a function of ball-milling time, and (c) lattice strain of the Fe crystallite as a function of milling time.

While these samples shown in Figure 6 contained 5 vol.% ZrC, the XRD peaks from this carbide phase was less pronounced than the Fe peaks because of its low volume fraction and nanoscale size (peak broadening). Nevertheless, the ZrC rocksalt structure's {111} reflection can be gleaned in the scans in Figure 6a from the modest increase in intensity seen near 65° 2θ .

Figure 7 is a set of representative SEM micrographs and EDS chemical maps of the NP dispersions from Route 2. Although some clear agglomeration is still present, the frequency and qualitative size of these larger features are dramatically reduced when comparing Figure 7a to Figure 5b. Increasing the magnification reveals the separation of finer NPs within the matrix, Figure 7b, which agrees with the EDS Zr signal map from the NPs in Figure 7c. These results support that the addition of the surfactant during the milling of the NPs and powders together does improve the NP dispersion.

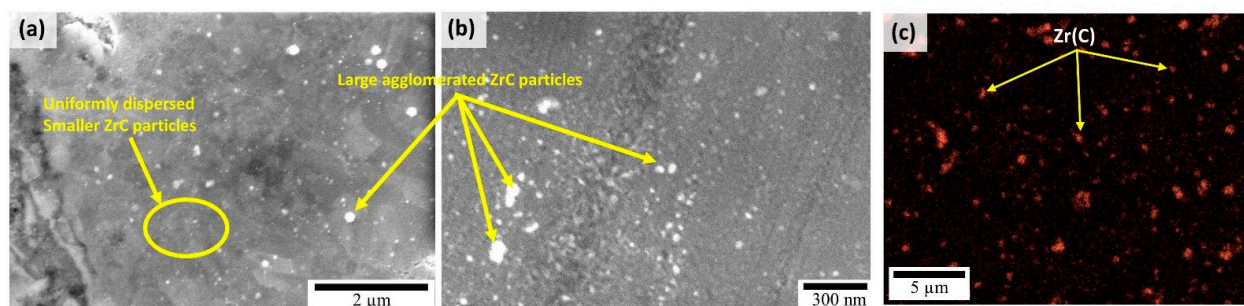


Figure 7. Fe-5 vol.% ZrC milled in Retsch mill for 6 h (a) SEM secondary electron image revealing the overall dispersion of the ZrC NPs (bright feature) (b) High magnification SEM secondary electron image, (c) EDS spectral map revealing Zr signals from the NPs.

3.3. Assessments of Route 3: Mixing of the Powders via a Liquid Solution

The aim of Route 3 was to mix all the necessary particulate components (powders plus NPs) into a suitable solution and determine if ball-milling was still necessary. To that end, the Fe powders, NPs, and PEI surfactant were mechanically mixed with ethanol creating a dispersion of the particulates in a liquid solution. The use of ethanol enabled the suspension solution to evaporate whereupon the mixed particulates would be sintered. Figure 8 are representative images of the NPs in the post-sintered state from this route. Although some larger agglomeration of the NPs is still present, they are smaller in size. It was also noticed that the density of the NPs was higher in some regions than others, Figure 8a,b. This was attributed to the evaporation of the ethanol solution, with the heavier particles (larger agglomerations) readily settling at the bottom. This difference was also noted between the overall Fe powders and NP clusters. Here, the Fe powders at or near the bottom that were pressed and sintered were found to have a qualitatively lower number of NPs within their microstructure than those from the upper portion of the consolidated sample. To mitigate this issue, the powders were mechanically shaken after drying, creating a much-improved dispersion of NPs through the sintered microstructure, Figure 8c,d.

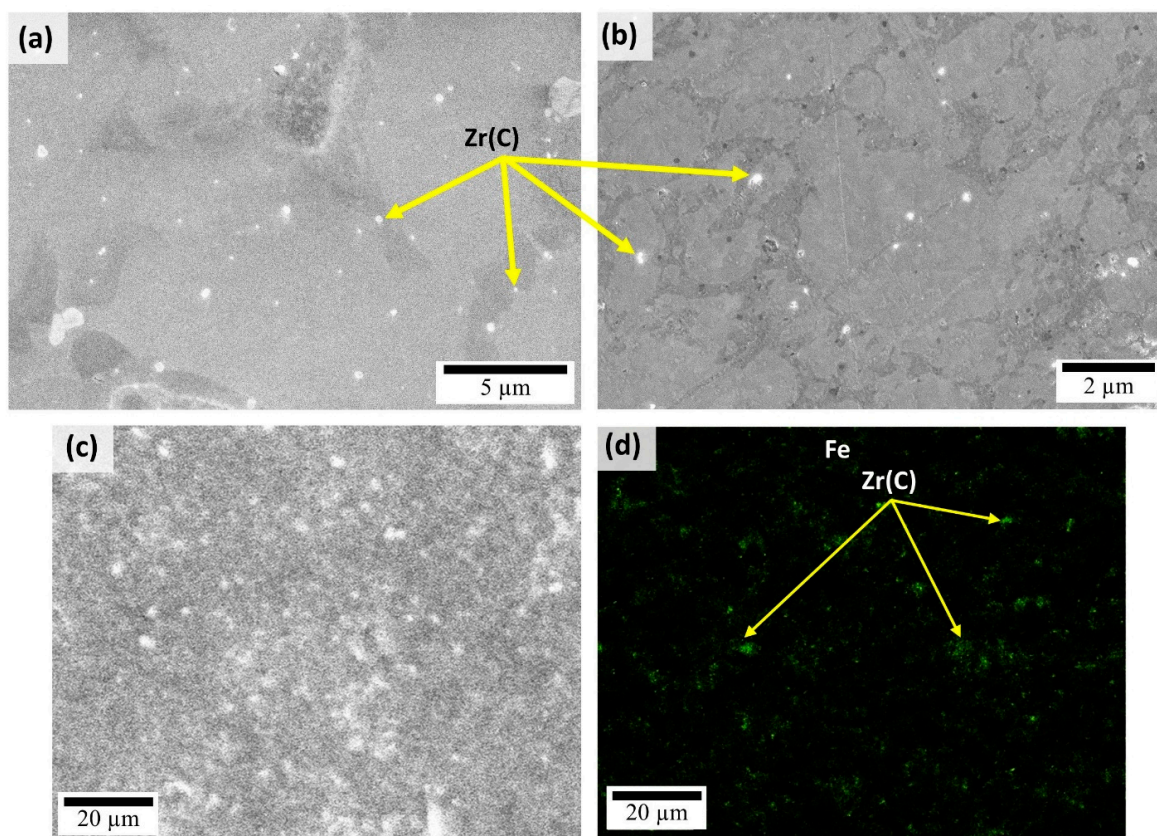


Figure 8. Nanoparticle dispersion in the metal matrix (a,b) SEM secondary electron micrographs of the sintered Fe-5 vol.% ZrC powder samples, (c) SEM secondary image of a selected area of the sintered sample that was mechanically shaken for 1 h (d) EDS signal map of Zr elements of the area presented in (c) showing the distribution of NPs.

3.4. Assessment of Route-4: Mechanochemical Processing on Solution-Mixed Powders

With the success of Route 3, this processing route was done to determine if ball-milling could further improve the de-agglomeration and dispersion of the NPs in the microstructure after drying the particles out of the liquid solution. Figure 9 are representative post-sintered micrographs of this dispersion. In each micrograph, the dispersion of the NPs is clear and relatively uniform. This suggests that a ball-milling step can indeed

further improve the uniformity of the NP dispersion after it has been mechanically mixed, dried, and re-shaken.

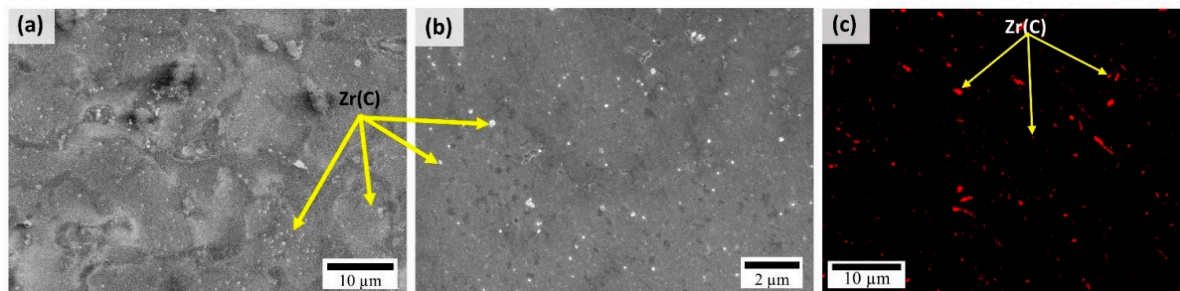


Figure 9. (a,b) SEM secondary electron micrographs of Fe-5 vol.% sintered samples produced by mechanochemical dispersion technique revealing the NP distribution (as the bright features), and (c) EDS elemental map of the Zr signal produced from ZrC particles.

3.5. Assessment of Route-5: Mechanochemical Processing on the Dispersed NPs

Although a surfactant has been shown to be an important chemical contributor to the dispersion of the NPs, to this point, it has been added in parallel with the Fe powders. The significant difference in the size of the powders versus the NPs would result in a significant fraction of the PEI being adsorbed onto the Fe powders. In this processing route, we aimed to target the PEI directly onto the NPs and then add the surfactant-coated NPs to the Fe powder mixture. Recognizing that an ethanol solution provides a means to mix the two types of particulates together, this would continue to be the initial mixing route prior to any ball-milling.

Figure 10 are the micrographs of the consolidated powders. It is quite clear from these images that the NPs have achieved a uniform dispersion throughout the microstructure with far fewer notable large-scale NP agglomerates as seen previously. This is more apparent in the EDS spatial map of the Zr signal, Figure 10d. Here, the sizes were $\approx 70 \pm 10$ nm and are on the order of the individual NP sizes placed in the mixture.

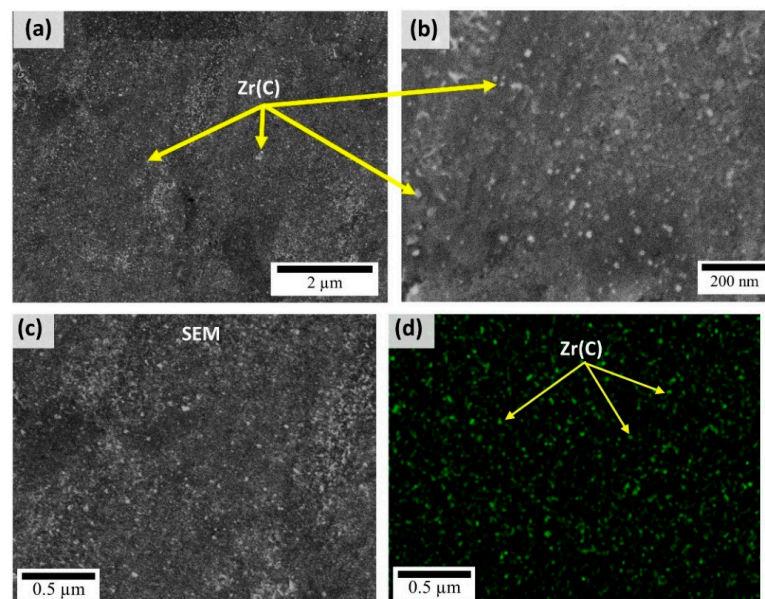


Figure 10. Nanoparticle dispersion in the Fe matrix (a,b) SEM secondary electron micrographs at progressive resolutions of the sintered Fe-5 vol.% ZrC powder samples, (c) SEM secondary electron micrograph of an area for collecting (d) EDS elemental map of Zr signals from ZrC showing the distribution of NPs.

4. Discussion

From each processing route, key features in how to disperse the NPs were determined. First, the higher ball-milling energy (Retsch mill) was more effective in breaking up and dispersing the NPs than a lower ball-milling process (Spex mill), Route 1, Figure 5. This is attributed to the increased impact energy the collective powder mixture experienced. Although a qualitative difference was noted, the high milling energy was still insufficient in reducing a significant number of agglomerated NPs in the sintered/consolidated sample. The incorporation of the PEI surfactant, Route 2, was then shown to help reduce the NP agglomerations but not eliminate it completely. Furthermore, the dispersion's uniformity was still problematic, Figure 7. Since the PEI was added directly with the Fe powders, it is likely that the Fe powders adsorbed a significant amount of the PEI on their surfaces reducing the PEI's direct impact on the NPs. Again, ball-milling was found to be insufficient in yielding a uniform dispersion of the NPs, whether as individual NPs or as smaller agglomerate 'clumps.' The inability to produce a uniform dispersion directly from ball-milling is attributed to the large particular size variation, with the NPs agglomerates being at least 10^3 sizes smaller than the Fe powders. Additionally, the stainless steel balls were multiple orders of magnitude larger in size than the Fe powders creating an even larger size disparity to the NPs. These extreme size differences between the particulates (powders and NPs) and the milling balls to the NPs likely contributed to the substantial difficulty in achieving a notable difference in uniform mixing between the powders and NPs with any direct ball milling process.

By placing the particulates into a liquid solution (Route 3 & 4), the particulates could then uniformly combine. By drying out the particles, this created a 'pre-mixed state' that then enabled the ball-milling to further break-up agglomerations, drive the dispersed NPs into the grains of the powders. This liquid solution mixing reduced the requirement for ball-milling to achieve the uniform dispersion, Figures 8 and 9.

Although the liquid solution pre-mix step was successful, the presence of NP agglomerates persisted, albeit qualitatively less than all previous routes. Recognizing that mixing the PEI with the Fe powders and ZrC NPs in the ethanol solution created similar agglomeration issues found in Route 2, Route 5 had the PEI surfactant directly applied to the NPs. The idea of which would be to mitigate the larger Fe powders dominating the PEI coverage. By ultrasonication, the NPs vibrated apart from each other allowing the PEI, which was in the ethanol solution, to flow around and be absorbed onto each NP. With PEI on the NP surface, placement of the dispersed NPs back into the ethanol solution with the Fe powders enabled the individual NPs to remain separated but now be dispersed in such a way to create a uniform mixture. By evaporating the ethanol solution away, a uniform mixture of particulates was achieved. These subsequent dry mixed particulates (powders and NPs) were then ball-milled to further drive the mixing and embed the NPs into the powders. This resulted in an individual NP dispersion that was uniformly decorating the sintered and consolidated microstructure, Figure 10. It is also worth to note that the high-energy ball-milling, with its creation of smaller and smaller crystallites within the powders, would bias the powder microstructure to coarsen around these ball-milled embedded NPs capturing them within their grain interiors. The inclusion of these uniformly dispersed NPs inside the grains will be instrumental in providing a desired strengthening mechanism. Finally, while sintering would result in a decomposition of the PEI surfactant as well as any residual ethanol on the powders, these products are simply composed of hydrocarbons making the Fe matrix a low carbon steel and may not necessarily be a detrimental outcome.

5. Conclusions

This study has reported various powder metallurgy processing routes for the incorporation of NPs into a sintered, consolidated microstructure using ZrC NPs and Fe powders as the case example. Each route, whether from direct ball mill mixing of powders to the incorporation of surfactants during milling to pre-mixing particulates in liquid solutions that were then subsequently dried and ball-milled, revealed key process outcomes in

what controls the NP dispersion in a powder metallurgy route. The results of our work reveal the critical importance in placing surfactants around the NPs prior to mixing, the use of particulate-liquid mixing, and finally ball-milling to embed and separate NPs prior to consolidation and sintering. The outcome of which is a powder processing route where tailored NP chemistries and/or morphologies can be directly incorporated into a microstructure. This is particularly relevant to systems where the chemistry, structure, and/or shape of the NP phase cannot be directly precipitated through conventional heat treatments. Consequently, tailored NPs can then be directly incorporated into metal matrices using conventional powder metallurgy processing routes to achieve new functionalities.

Author Contributions: Conceptualization of the process completed by B.P.R., C.R.W. and G.B.T. B.P.R. completed experiments, data analysis, and original draft preparation with edits by coauthors. C.R.W., S.R.D. and G.B.T. acquired the funding for this project. All authors have read and agreed to the published version of the manuscript.

Funding: This research project was funded by the US Department of Energy (DOE), Grant number DE-EE0008831. The authors thank Jonathan Priedeman for reviewing the manuscript and providing comments.

Institutional Review Board Statement: Not applicable.

Informed Consent Statement: Not applicable.

Data Availability Statement: The data presented in this study are available from the corresponding author, upon reasonable request.

Conflicts of Interest: The authors declare no conflict of interest.

References

1. Malaki, M.; Xu, W.; Kasar, A.K.; Menezes, P.L.; Dieringa, H.; Varma, R.S.; Gupta, M. Advanced metal matrix nanocomposites. *Metals* **2019**, *9*, 330. [[CrossRef](#)]
2. Huang, X.; Qi, X.; Boey, F.; Zhang, H. Graphene-based composites. *Chem. Soc. Rev.* **2011**, *41*, 666–686. [[CrossRef](#)] [[PubMed](#)]
3. Riedel, R. Nanoscaled inorganic materials by molecular design. *Chem. Soc. Rev.* **2012**, *41*, 5029. [[CrossRef](#)]
4. Soltani, N.; Sadrnezhaad, S.K.; Bahrami, A. Manufacturing wear-resistant 10Ce-TZP/Al₂O₃ nanoparticle aluminum composite by powder metallurgy processing. *Mater. Manuf. Process.* **2014**, *29*, 1237–1244. [[CrossRef](#)]
5. Pham, V.T.; Bui, H.T.; Tran, B.T.; Nguyen, V.T.; Le, D.Q.; Than, X.T.; Doan, D.P.; Phan, N.M. The effect of sintering temperature on the mechanical properties of a Cu/CNT nanocomposite prepared via a powder metallurgy method. *Adv. Nat. Sci. Nanosci. Nanotechnol.* **2011**, *2*, 015006. [[CrossRef](#)]
6. Zhang, W.; Hu, Y.; Wang, Z.; Yang, C.; Zhang, G.; Prashanth, K.; Suryanarayana, C. A novel high-strength Al-based nanocomposite reinforced with Ti-based metallic glass nanoparticles produced by powder metallurgy. *Mater. Sci. Eng. A* **2018**, *734*, 34–41. [[CrossRef](#)]
7. Zhou, X.; Su, D.; Wu, C.; Liu, L. Tensile mechanical properties and strengthening mechanism of hybrid carbon nanotube and silicon carbide nanoparticle-reinforced magnesium alloy composites. *J. Nanomater.* **2012**, *2012*, 1–7. [[CrossRef](#)]
8. Shi, R.-J.; Wang, Z.-D.; Qiao, L.-J.; Pang, X.-L. Effect of in-situ nanoparticles on the mechanical properties and hydrogen embrittlement of high-strength steel. *Int. J. Miner. Met. Mater.* **2021**, *28*, 644–656. [[CrossRef](#)]
9. Cho, L.; Seo, E.J.; Sulistiyo, D.H.; Jo, K.R.; Kim, S.W.; Oh, J.K.; Cho, Y.R.; De Cooman, B.C. Influence of vanadium on the hydrogen embrittlement of aluminized ultra-high strength press hardening steel. *Mater. Sci. Eng. A* **2018**, *735*, 448–455. [[CrossRef](#)]
10. Depover, T.; Verbeken, K. Hydrogen trapping and hydrogen induced mechanical degradation in lab cast Fe-C-Cr alloys. *Mater. Sci. Eng. A* **2016**, *669*, 134–149. [[CrossRef](#)]
11. Ghosh, K.; Mondal, D. Effect of grain size on mechanical electrochemical and hydrogen embrittlement behaviour of a micro-alloy steel. *Mater. Sci. Eng. A* **2013**, *559*, 693–705. [[CrossRef](#)]
12. Bhadeshia, H.K.D.H. Prevention of hydrogen embrittlement in steels. *ISIJ Int.* **2016**, *56*, 24–36. [[CrossRef](#)]
13. Chen, L.-Y.; Xu, J.-Q.; Choi, H.; Pozuelo, M.; Ma, X.; Bhowmick, S.; Yang, J.-M.; Mathaudhu, S.; Li, X.-C. Processing and properties of magnesium containing a dense uniform dispersion of nanoparticles. *Nat. Cell Biol.* **2015**, *528*, 539–543. [[CrossRef](#)]
14. Mackay, M.E.; Tuteja, A.; Duxbury, P.M.; Hawker, C.J.; Van Horn, B.; Guan, Z.; Chen, G.; Krishnan, R.S. General strategies for nanoparticle dispersion. *Science*. **2006**, *311*, 1740–1743. [[CrossRef](#)] [[PubMed](#)]
15. Korayem, A.; Tourani, N.; Zakertabrizi, M.; Sabziparvar, A.; Duan, W. A review of dispersion of nanoparticles in cementitious matrices: Nanoparticle geometry perspective. *Constr. Build. Mater.* **2017**, *153*, 346–357. [[CrossRef](#)]
16. Machado, B.B.; Scabini, L.F.; Orue, J.P.M.; De Arruda, M.S.; Goncalves, D.N.; Goncalves, W.N.; Moreira, R.; Rodrigues, J.F., Jr. A complex network approach for nanoparticle agglomeration analysis in nanoscale images. *J. Nanopart. Res.* **2017**, *19*, 65. [[CrossRef](#)]

17. Sokolov, S.V.; Tschulik, K.; Batchelor-McAuley, C.; Jurkschat, K.; Compton, R.G. Reversible or not? Distinguishing agglomeration and aggregation at the nanoscale. *Anal. Chem.* **2015**, *87*, 10033–10039. [[CrossRef](#)] [[PubMed](#)]
18. Suttiponparnit, K.; Jiang, J.; Sahu, M.; Suvachittanont, S.; Charinpanitkul, T.; Biswas, P. Role of surface area, primary particle size, and crystal phase on titanium dioxide nanoparticle dispersion properties. *Nanoscale Res. Lett.* **2010**, *6*, 27. [[CrossRef](#)]
19. Loza, K.; Epple, M.; Maskos, M. Stability of nanoparticle dispersions and particle agglomeration. In *2D Nanoelectronics*; Springer Science and Business Media LLC: New York, NY, USA, 2019; pp. 85–100.
20. Shang, X.; Wang, X.; Chen, S. Effects of ball milling processing conditions and alloy components on the synthesis of Cu-Nb and Cu-Mo alloys. *Materials* **2019**, *12*, 1224. [[CrossRef](#)] [[PubMed](#)]
21. Ilyas, S.U.; Pendyala, R.; Marneni, N. Preparation, sedimentation, and agglomeration of nanofluids. *Chem. Eng. Technol.* **2014**, *37*, 2011–2021. [[CrossRef](#)]
22. Razavi-Tousi, S.S.; Szpunar, J.A. Role of ball milling of aluminum powders in promotion of aluminum-water reaction to generate hydrogen. *Met. Mater. Trans. E* **2014**, *1*, 247–256. [[CrossRef](#)]
23. Sarwat, S.G. Contamination in wet-ball milling. *Powder Met.* **2017**, *60*, 267–272. [[CrossRef](#)]
24. Toozandehjani, M.; Matori, K.A.; Ostovan, F.; Aziz, S.A.; Mamat, S. Effect of milling time on the microstructure, physical and mechanical properties of Al-Al₂O₃ nanocomposite synthesized by ball milling and powder metallurgy. *Materials* **2017**, *10*, 1232. [[CrossRef](#)] [[PubMed](#)]
25. López-García, J.; Sánchez-Alarcos, V.; Recarte, V.; Rodríguez-Velamazán, J.; Unzueta, I.; Plazaola, F.; La Roca, P.; Pérez-Landazábal, J. Effect of high-energy ball-milling on the magnetostructural properties of a Ni₄₅Co₅Mn₃₅Sn₁₅ alloy. *J. Alloys Compd.* **2021**, *858*, 158350. [[CrossRef](#)]
26. Cipolloni, G.; Pellizzari, M.; Molinari, A.; Hebda, M.; Zadra, M. Contamination during the high-energy milling of atomized copper powder and its effects on spark plasma sintering. *Powder Technol.* **2015**, *275*, 51–59. [[CrossRef](#)]
27. Suryanarayana, C. Mechanical alloying and milling. *Prog. Mater. Sci.* **2001**, *46*, 1–184. [[CrossRef](#)]
28. Bolsonella, A.; Naimi, F.; Heintz, O.; Tricone, T.; Couque, H.; Bernard, F. Influence of oxygen induced during high-energy ball milling process on the mechanical properties of sintered nickel by SPS. *J. Alloys Compd.* **2021**, *856*, 157869. [[CrossRef](#)]
29. Im, T.; Pyo, J.; Lee, J.-S.; Lee, C.S. Fabrication of homogeneous nanosized nickel powders using a planetary ball mill: Applications to multilayer ceramic capacitors (MLCCs). *Powder Technol.* **2021**, *382*, 118–125. [[CrossRef](#)]
30. Caicedo, F.M.C.; López, E.V.; Agarwal, A.; Drozd, V.; Durygin, A.; Hernandez, A.F.; Wang, C. Synthesis of graphene oxide from graphite by ball milling. *Diam. Relat. Mater.* **2020**, *109*, 108064. [[CrossRef](#)]
31. Rogal, Ł.; Kalita, D.; Tarasek, A.; Bobrowski, P.; Czerwinski, F. Effect of SiC nano-particles on microstructure and mechanical properties of the CoCrFeMnNi high entropy alloy. *J. Alloys Compd.* **2017**, *708*, 344–352. [[CrossRef](#)]
32. Suryanarayana, C.; Ivanov, E. Mechanochemical synthesis of nanocrystalline metal powders. In *Advances in Powder Metallurgy*; Elsevier: Amsterdam, The Netherlands, 2013; pp. 42–68.
33. Gilstrap, R.A.; Capozzi, C.J.; Carson, C.G.; Gerhardt, R.A.; Summers, C.J. Synthesis of a nonagglomerated indium tin oxide nanoparticle dispersion. *Adv. Mater.* **2008**, *20*, 4163–4166. [[CrossRef](#)]
34. Chen, D.; Jiang, Y.; Cai, J.-G.; Chen, Z.-H.; Huang, P.-Y. Production of intermetallic compound powders by a mechanochemical approach: Solid–liquid reaction ball milling. In *High-Energy Ball Milling*; Elsevier: Amsterdam, The Netherlands, 2010; pp. 149–166.
35. El-Nour, K.M.A.; Eftaiha, A.; Al-Warthan, A.; Ammar, R.A. Synthesis and applications of silver nanoparticles. *Arab. J. Chem.* **2010**, *3*, 135–140. [[CrossRef](#)]
36. Zhu, X.; Tang, F.; Suzuki, T.S.; Sakka, Y. Role of the initial degree of ionization of polyethylenimine in the dispersion of silicon carbide nanoparticles. *J. Am. Ceram. Soc.* **2003**, *86*, 189–191. [[CrossRef](#)]
37. Nomura, Y.; Iijima, M.; Kamiya, H. Hydrophobic group functionalization of polyethyleneimine for controlling dispersion behavior of silicon carbide nanoparticles in aqueous suspension. *J. Am. Ceram. Soc.* **2012**, *95*, 3448–3454. [[CrossRef](#)]
38. Vilinska, A.; Ponnurangam, S.; Chernyshova, I.; Somasundaran, P.; Eroglu, D.; Martinez, J.; West, A.C. Stabilization of Silicon Carbide (SiC) micro- and nanoparticle dispersions in the presence of concentrated electrolyte. *J. Colloid Interface Sci.* **2014**, *423*, 48–53. [[CrossRef](#)]
39. Kowalski, A.J.; Watson, S.; Wall, K. Dispersion of nanoparticle clusters by ball milling. *J. Dispers. Sci. Technol.* **2008**, *29*, 600–604. [[CrossRef](#)]
40. Afkham, Y.; Khosroshahi, R.A.; Mousavian, R.T.; Brabazon, D.; Kheirifard, R. Microstructural characterization of ball-milled metal matrix nanocomposites (Cr, Ni, Ti)-25 wt% (Al₂O₃np, SiCnp). *Part. Sci. Technol.* **2016**, *36*, 72–83. [[CrossRef](#)]
41. Suryanarayana, C.; An, I.-S. Mechanical alloying and milling. *J. Korean Powder Met. Inst.* **2006**, *13*, 371–372. [[CrossRef](#)]
42. Shiraiishi, M.; Inagaki, M. X-ray diffraction methods to study crystallite size and lattice constants of carbon materials. In *Carbon Alloys*; Elsevier: Amsterdam, The Netherlands, 2003; pp. 161–173.